sPHENIX Conference Note

tag: sPH-CONF-JET-2025-05
version: 1.0
DOI: unspecified
date: September 4, 2025

sPHENIX Conference Note

...

Measurement of dijet momentum balance in Au+Au collisions at $\sqrt{s_{\rm NN}} = 200$ GeV with the sPHENIX detector

sPHENIX Collaboration

Abstract

This sPHENIX Conference Note details the measurement of dijet momentum balance (x_J) in Au+Au collision data at $\sqrt{s_{\rm NN}} = 200$ GeV taken with the sPHENIX detector in 2024 at the Relativistic Heavy Ion Collider. Jets are reconstructed using the anti-k_t algorithm with $R = 0.3$ from electromagnetic and hadronic calorimeter energy deposits, constituting the first full calorimeter jet measurement in heavy-ion collisions at RHIC. The measurement is performed in 0.1 nb^{-1} of collision data, corresponding to a small fraction of the expected Au+Au data collected in 2025. Events where the leading jet has $p_{T,1}$= 30–43.2 GeV, and is azimuthally back-to-back ($\Delta\phi > 7\pi/8$) with the highest sub-leading jet that has $p_{T,2}>$ 10.1 GeV, are used for analysis. The pair-normalized distributions are corrected for combinatoric background, unfolded for detector effects back to the truth-particle level, and reported in different Au+Au centrality intervals (0–10%, 10–30%, 30–50%, 50–90%). The x_J distributions are significantly modified in central Au+Au collisions compared to those in p+p collisions as a consequence of jet-medium interactions with the quark–gluon plasma. The results are compared to a selection of theoretical predictions.

1 Introduction

Hard scattered quarks and gluons traversing the quark-gluon plasma (QGP) have significantly modified parton showers. Their energy is shifted to larger angles away from the parton because of interactions with the medium and can also be transferred to the medium itself; see, for example, Ref. [1]. Dijet asymmetry measurements at the Large Hadron Collider (LHC) indicate substantial jet quenching in Pb+Pb collisions relative to p+p collisions as the vacuum baseline [2, 3, 4]. Initial dijet measurements, without unfolding for detector effects to the truth-particle level, have also been performed by the STAR experiment at the Relativistic Heavy Ion Collider (RHIC) [5]. These results have generated significant theoretical interest in understanding their origin and systematic dependence [6, 7, 8].

The sPHENIX Collaboration has previously measured the dijet momentum balance in p+p collisions at $\sqrt{s} = 200$ GeV, fully unfolded for detector effects [9]. These results were reported for $R = 0.4$ jets and characterized by the ratio $x_J = p_{T,2}/p_{T,1}$, where $p_{T,1}$ and $p_{T,2}$ correspond to the leading and sub-leading jet in the event, respectively. Notably, the x_J distributions are normalized per dijet pair, i.e., to unity integral. The analysis presented here extends these measurements to centrality-selected Au+Au collisions at $\sqrt{s_{\rm NN}} = 200$ GeV taken with the sPHENIX detector in 2024 at RHIC.

This note presents a measurement of the dijet momentum balance (x_J) distributions in Run 2024 Au+Au data. Results are reported in centrality intervals of 0–10%, 10–30%, 30–50%, and 50–90%, corresponding to central, mid-central, mid-peripheral, and peripheral collisions, respectively. The analysis is performed using anti-k_t jets with radius parameter $R = 0.3$ [10], and the distributions are unfolded within the kinematic selection $p_{T,1}$= 30–43.2 GeV, $p_{T,2} > 10.1$ GeV, and requiring the azimuthal separation ($\Delta\phi$) between these jets to be greater than $7\pi/8$. The Run 2024 p+p data are also reprocessed, following the identical procedure detailed in Ref. [9], to apply the same R value and kinematic selections. The Au+Au and p+p integrated luminosities correspond to approximately 0.1 nb^{-1} and 25 pb^{-1}, respectively.

2 sPHENIX Detector

sPHENIX [11, 12] is a new detector at RHIC [13] designed to measure jet and heavy-flavor probes of the QGP created in Au+Au collisions. A precision tracking system enables measurements of heavy-flavor and jet-substructure observables while the electromagnetic and hadronic calorimeter systems are used for measuring the energy of jets and identifying direct photons and electrons.

Going outwards starting from the beam line, sPHENIX comprises the following subsystems [14]: the MAPS-based Vertex Detector (MVTX); the INTermediate Tracker (INTT); the Time Projection Chamber (TPC) [15]; the Time Projection Chamber Outer Tracker (TPOT) [16]; the Electromagnetic Calorimeter (EMCAL) [17, 18]; the Inner Hadronic Calorimeter (IHCAL) [18]; the 1.4 T superconducting solenoid magnet [19] and the Outer Hadronic Calorimeter (OHCAL) [18]. Except for TPOT, all detectors have full azimuthal coverage and span $|\eta| < 1.1$ in pseudorapidity. sPHENIX also includes a number of forward detectors, namely the Minimum Bias Detectors (MBD), the sPHENIX Event Plane Detectors (sEPD), and the Zero Degree Calorimeters (ZDC), that includes the Shower Maximum Detector (SMD).

sPHENIX began its commissioning process in RHIC Run-2023 with Au+Au collisions at $\sqrt{s_{\rm NN}} =$ 200 GeV. During RHIC Run-2024, sPHENIX collected a large sample of transversely polarized p+p physics data at $\sqrt{s} = 200$ GeV alongside a smaller sample of Au+Au data to complete its commissioning phase in that collision system. Currently in 2025, sPHENIX is accumulating a large luminosity of Au+Au collision data.

3 Analysis Procedure

The data used for this analysis were collected in RHIC Run 2024 Au+Au $\sqrt{s_{\rm NN}} = 200$ GeV running. Events are selected by requiring the coincidence of hits in at least two photomultiplier tubes in each side of the MBD. Selections on the correlation of the MBD charge between both sides, and on the energies in the two ZDC sides, are applied to remove non-collision and beam backgrounds. The collision centrality is characterized by the total charge in the two MBD sides, with the trigger and offline selection requirements corresponding to $93 \pm 3\%$ of the total Au+Au inelastic cross-section [20]. The z-vertex position is determined by the timing difference between the two halves of the MBD. Its typical width for runs in this dataset is 15 cm and all events with $|z| < 60$ cm are accepted. These selections yield approximately 650 million minimum-bias Au+Au events for the analysis.

Monte Carlo (MC) simulations of jet production in a Au+Au collision background are used to evaluate the performance of jet measurements and correct for detector effects on the measured jet kinematics. Pythia-8 [21] jet events are generated with the "HardQCD:all" and "PromptPhoton:all" processes for various $\hat{p}_{\rm T}^{\rm min}$ thresholds to span a large kinematic range, using the Detroit tune [22] optimized for RHIC-energy jet observables.

The Au+Au background is simulated using Hijing [23], with a flow afterburner procedure which adjusts the momentum of final-state particles to match the average v_n values previously measured at RHIC as a function of centrality, p_T, and pseudorapidity [24, 25]. The Hijing simulations are generated with a z-vertex distribution similar to that in the Run 2024 Au+Au data sample, and the embedded Pythia-8 event is placed at the position of the Hijing event. The combined Pythia-8 plus Hijing event is propagated through a full description of the sPHENIX detector using the Geant-4 simulation package [26] and reconstructed in a manner similar to the data. The simulation samples are reweighted in centrality and z-vertex position to match the distributions of those quantities for jet events in Au+Au data, and the jet energy resolution is adjusted to match that observed in Run 2024 p+p data using the dijet bisector method [9].

Jets are reconstructed according to the anti-k_t algorithm [10] with $R = 0.3$ using the energy deposited in $\Delta\eta \times \Delta\phi = 0.1 \times 0.1$ calorimeter towers in the EMCAL and HCALs. A two-step procedure is used to estimate and subtract the underlying event (UE) in Au+Au collisions, which closely follows that outlined in Ref. [27]. In the first step, unsubtracted towers are clustered into anti-k_t $R = 0.2$ jets, and the subset of those jets with at least one tower above 3 GeV and a maximum-to-average tower energy ratio greater than three is used to define regions consistent with jet production ("seed jets"). A ϕ-averaged UE energy density is determined in each $\Delta\eta = 0.1$ slice and for each of the three calorimeter layers, excluding towers that are within $\Delta R < 0.4$ of a seed jet. The seed jet kinematics are then updated by subtracting, tower by tower, the estimated UE energy density in that η slice and calorimeter layer. In the next iteration, seed jets that have p_T

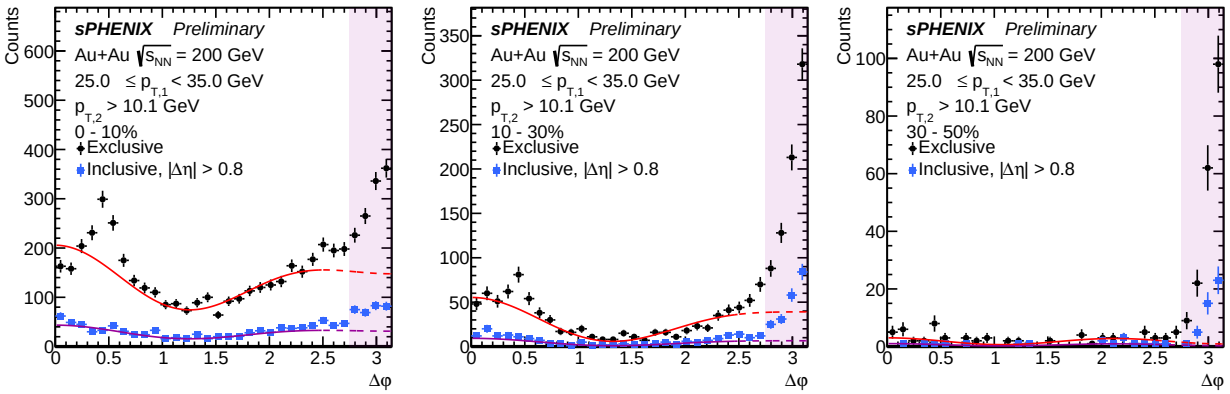

Figure 1: Examples of the combinatoric background subtraction procedure for selected $p_{T,1} \otimes p_{T,2}$ ranges and centralities. Shown are the $\Delta\phi$ distributions for exclusive dijet pairs (black points) and inclusive pairs separated by $|\Delta\eta| > 0.8$ (blue points). The lower magenta curve shows the Fourier fit to the inclusive distribution which is used to set the $\Delta\phi$ shape, and the upper red curve shows the estimated background in the exclusive distribution, including in the signal region $\Delta\phi > 7\pi/8$ (shaded pink). See text for details.

> 7 GeV after subtraction are used to define a new set of seeds. The UE energy density is again determined, now excluding towers within $\Delta R < 0.4$ of the second set of seed jets. Finally, all calorimeter towers are corrected to account for this second estimate of the UE energy density, and jet reconstruction with $R = 0.3$ is run to determine the final subtracted jet kinematics. Importantly, the procedure used in this analysis determines a ϕ-averaged estimate of the UE energy density, and does not attempt to correct for the event-by-event hydrodynamic flow which introduces a modulation of this quantity in ϕ. The impact of flow on the reconstructed jet response is corrected for in the unfolding procedure described below.

Reconstructed jets are required to be within $|\eta_{\text{jet}}| < 0.8$ to ensure full containment within the calorimeter system. Events with a leading (highest-p_T) jet with $p_{T,1}$= 30–43.2 GeV are selected for analysis. Other jets in the event are required to have $p_{T,2}>$ 10.1 GeV to ensure a reliable measurement of jet kinematics despite the significant Au+Au UE background. The particular choice of p_T binning is determined by the need to project the resulting $p_{T,1} \otimes p_{T,2}$ distribution down to a one-dimensional x_J distribution. The main analysis selection is an "exclusive" selection, using only the second-highest-p_T jet as the subleading jet partner to the leading jet. However, an "inclusive" selection, defined by pairing the leading jet with each of the possible additional jets above 10.1 GeV in the event, is also used in the analysis for estimating the combinatorial jet background contribution and as a systematic check.

Dijet pairs in Au+Au events can have a significant contribution from the combinatoric pairing of a leading jet from a hard scattering with a "fake" (UE fluctuation) jet or otherwise unrelated jet, or from two such jets. This contribution is estimated in a data-driven way using sideband regions in $\Delta\phi$ and statistically subtracted from the signal yield in the region $\Delta\phi > 7\pi/8$, separately in different ranges of $p_{T,1} \otimes p_{T,2}$. The combinatoric jet contribution is expected to have a non-flat shape in $\Delta\phi$ due to the influence of hydrodynamic flow.

Figure 1 shows examples of the $\Delta\phi$ distribution in different centrality selections. The distributions have a depletion around $\Delta\phi \approx 0$ and a peak at $\Delta\phi \approx 2R \approx 0.6$, since two anti-$k_t$ jets cannot gener-

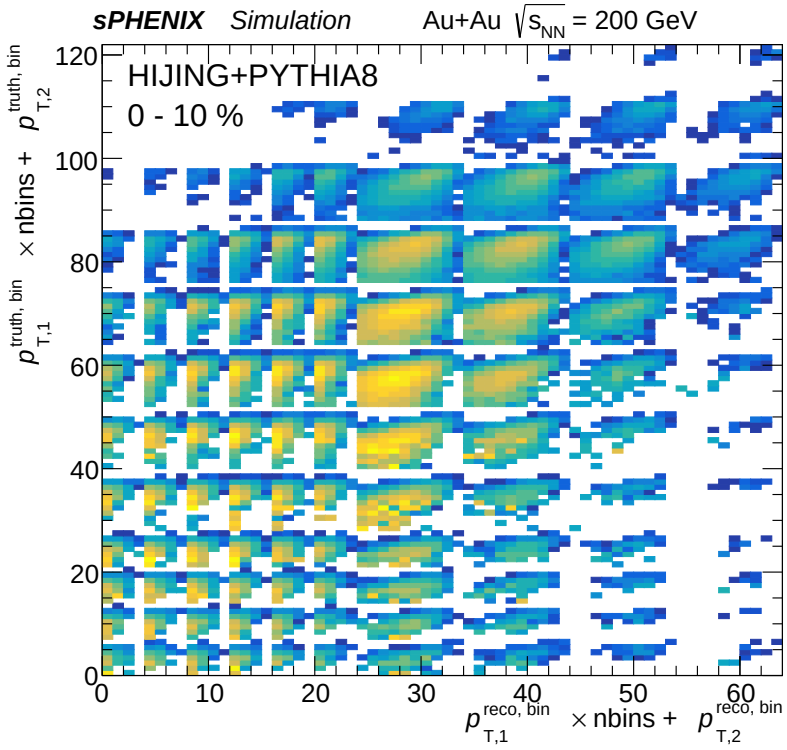

Figure 2: Response matrix for PYTHIA-8 jets embedded into HIJING Au+Au background, shown for 0–10% events. The x- and y-axis indices correspond to reco- and truth-particle level $p_{T,1} \otimes p_{T,2}$ bins. The entries in each bin are shown on a logarithmic scale.

ally be reconstructed within $\Delta R < R$ and thus the next-nearest position is at approximately twice the jet radius. These features prohibit an extraction of the flow modulation of the combinatoric jet yield.

Thus, the shape of the combinatoric $\Delta\phi$ distribution is determined using an "inclusive" selection of all possible subleading jets in the given $p_{T,2}$ range, where only jets separated from the leading jet by $|\Delta\eta| > 0.8$ are considered. As seen in Figure 1, this selection removes the near-side depletion and nearby-jet contribution. This $\Delta\phi$ distribution is fit to a functional flow form with $v_{2,2}$ and $v_{3,3}$ components in the range $0 < \Delta\phi < 2.5$ to model the shape of the contribution from combinatoric jet pairs. This functional form is then applied to the "exclusive" $p_{T,1} \otimes p_{T,2}$ selection, where it is scaled to match the average of the distribution in the region $0.8 < \Delta\phi < 2.5$. The integral of the function in the region $\Delta\phi > 7\pi/8$ is taken as the estimate of the combinatoric contribution to the signal, and is subtracted from the yield measured in that $p_{T,1} \otimes p_{T,2}$ selection.

After this background subtraction, the distributions are corrected for the inefficiency arising from a combinatoric jet having a higher p_T and thus displacing a hard-scattering associated away-side jet in the exclusive selection. This correction is determined from the per-event jet yields in minimum-bias Au+Au data and is applied as a function of $p_{T,2}$. The inefficiency is approximately 50% for the lowest-$p_{T,2}$ selection in the most central events, but rises quickly with increasing $p_{T,2}$ or less central event selections.

An unfolding procedure utilizing the iterative Bayesian algorithm [28] in the RooUnfold package [29] is used to correct for detector effects in the x_J measurement, including bin migration and kinematic selection inefficiency. The procedure follows closely from that used in the previous measurement of dijet x_J in p+p collisions [9] and is summarized below. For each centrality interval, four-dimensional response matrices are populated for bin migration of the yield as a function of $p_{T,1} \otimes p_{T,2}$ from the truth-particle to reconstructed levels, for the two highest-p_T jets that have $\Delta\phi > 7\pi/8$. An example response matrix is shown in Figure 2. These prior distributions are reweighted by the observed $p_{T,1} \otimes p_{T,2}$ distributions at the reconstructed level in Au+Au data. The number of iterations in the unfolding procedure is chosen by optimizing the combination of the statistical uncertainty and the change in the results with respect to the previous iteration, separately for each centrality. After unfolding, the truth-particle level $p_{T,1} \otimes p_{T,2}$ distributions are projected to one-dimensional x_J distributions.

4 Systematic Uncertainties

The main sources of systematic uncertainty in the x_J measurement include: the jet energy scale (JES), the jet energy resolution (JER), the combinatoric background subtraction, the subleading efficiency, and the unfolding for detector effects. The JES and JER uncertainties include the uncertainties in the absolute calorimeter response to p+p-like jets previously discussed in Ref. [9], as well as additional components accounting for the measurement of jets in the Au+Au dataset. These include the modeling of the UE fluctuations in simulation, which is studied by comparing the transverse energy distribution in random cones in data and simulation, and the potentially different calorimeter response to the modified fragmentation of quenched jets, evaluated by comparing the response of quark versus gluon jets in simulation. The uncertainty in the combinatoric background subtraction procedure is evaluated by assuming a flat contribution in $\Delta\phi$, determined from the exclusive $\Delta\phi$ distribution, rather than a flow-modulated one, and by repeating the analysis with an inclusive dijet definition of the observable. The uncertainty on the subleading efficiency is quantified by performing the analysis with inclusive subleading jets (all jets that meet the minimum subleading jet p_T cut). Allowing all possible subleading jets makes the subleading efficiency unnecessary, and the addition of the combinatoric background is subtracted by the combinatoric background subtraction. The uncertainty in the unfolding is determined by removing the significant reweighting of the prior in simulation before unfolding. The systematic uncertainties included in the p+p result are identical to the listed uncertainties in Ref. [9] but are reprocessed with the kinematic selection and jet R value used in this measurement.

The magnitudes of individual uncertainty sources and the total uncertainty are shown for two example centrality intervals in Figure 3. Due to the self-normalization of the observable, the uncertainties are anti-correlated between low and high x_J regions, with a minimum around the median x_J value. The dominant source of uncertainty varies depending on the centrality interval and the x_J region. Additionally, the uncertainties related to statistical uncertainties in the simulation samples are added in quadrature with those on the data and are reported together as vertical bars in the following Figures.

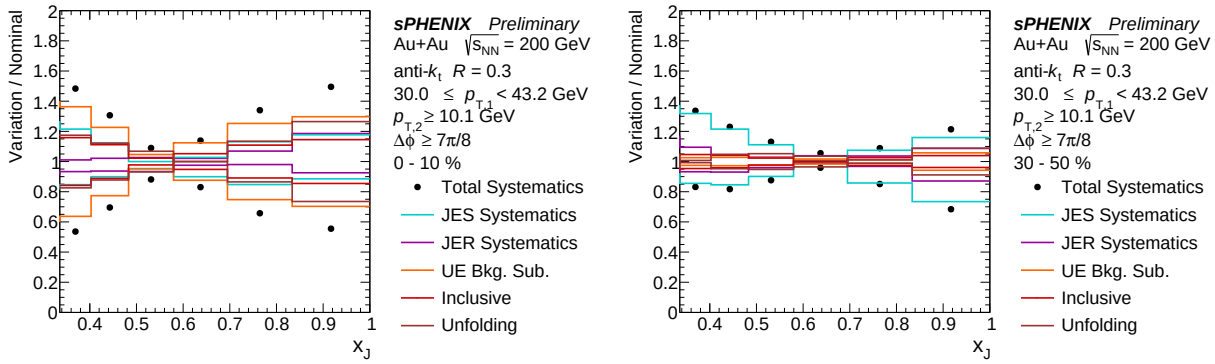

Figure 3: Summary of the magnitudes of different systematic uncertainty components and the total uncertainty for the x_J measurement in 0–10% (left) and 30–50% (right) Au+Au collisions.

5 Results

Figure 4 shows the fully corrected x_J distributions for events where the leading jet lies in the range $30.0 \leq p_{T,1} < 43.2$ GeV, the subleading jet satisfies $p_{T,2} > 10.1$ GeV, and the azimuthal back-to-back selection $\Delta\phi > 7\pi/8$ is applied. In this selection, the subleading jet is exclusively the second-highest p_T jet in the entire event, i.e., at any η, ϕ angle. The distributions are normalized per selected dijet pair. The results are shown for Au+Au centrality intervals 0–10%, 10–30%, 30–50%, and 50–90%, as well as for p+p collisions. In the most peripheral Au+Au events, the x_J distribution is compatible with that in p+p collisions within the combined uncertainties of each measurement. However, in the other three centrality intervals, the shape of the x_J distribution in Au+Au collisions is significantly modified compared to p+p or peripheral collisions, with a relative suppression at large x_J values and relative enhancement at low x_J values.

Figure 5 shows all Au+Au centrality intervals and p+p data overlaid. The x_J distributions for the 0–10%, 10–30%, and 30–50% Au+Au events have a trend towards larger modification in more central events, though are just compatible within uncertainties. In contrast, the 50–90% and p+p distributions are significantly different. Notably, the reported observable is normalized per surviving dijet pair, and thus the similar x_J distributions for the three most central event selections do not necessarily imply a similar level of overall jet suppression.

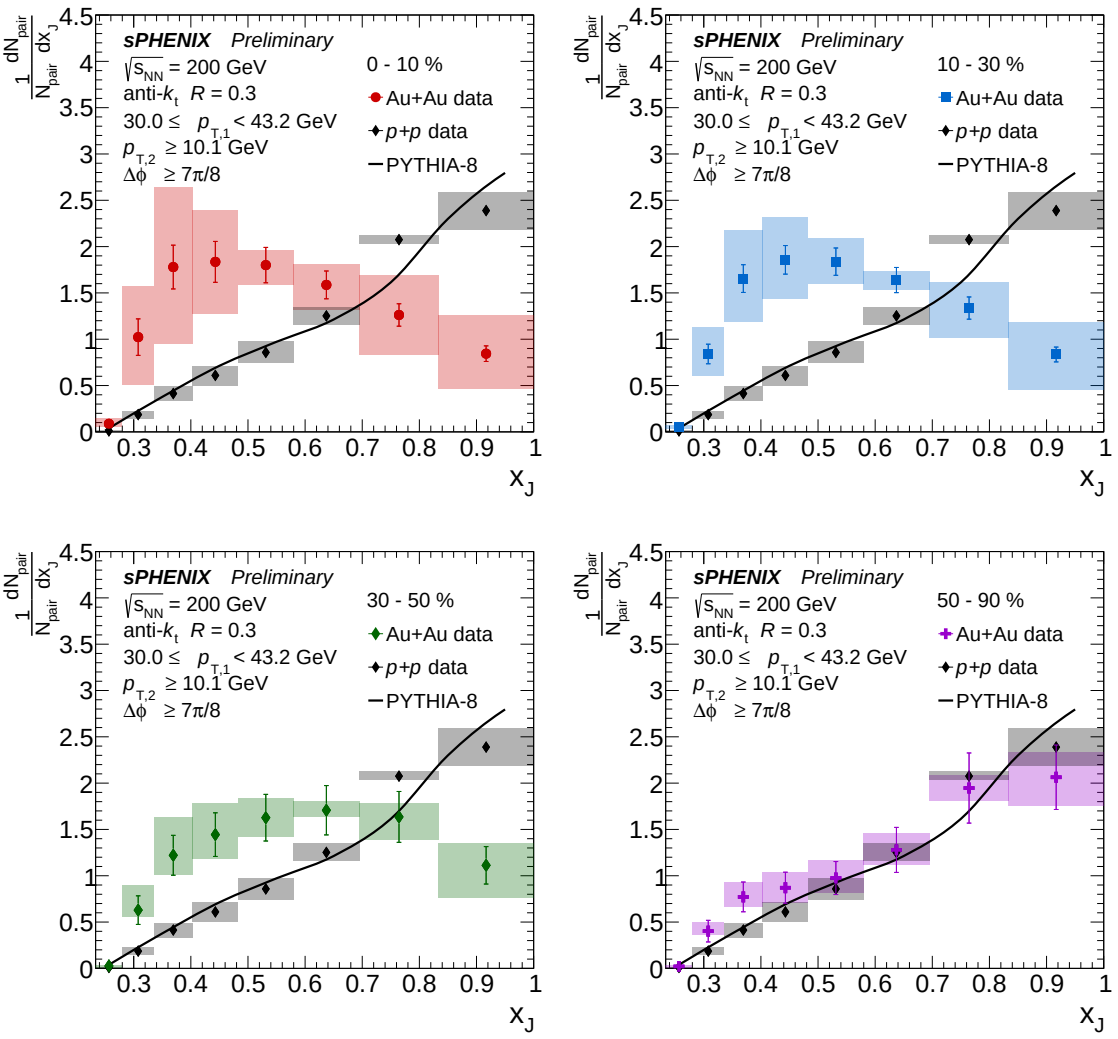

Figure 4: Fully unfolded x_J distributions of dijet events are shown for different Au+Au collision centrality intervals in each panel: 0–10%, 10–30%, 30–50%, and 50–90%. The x_J distributions in p+p collisions and in PYTHIA-8 are shown on each panel with matching kinematic selections. For the data distributions, statistical uncertainties are shown as vertical lines and systematic uncertainties as filled boxes.

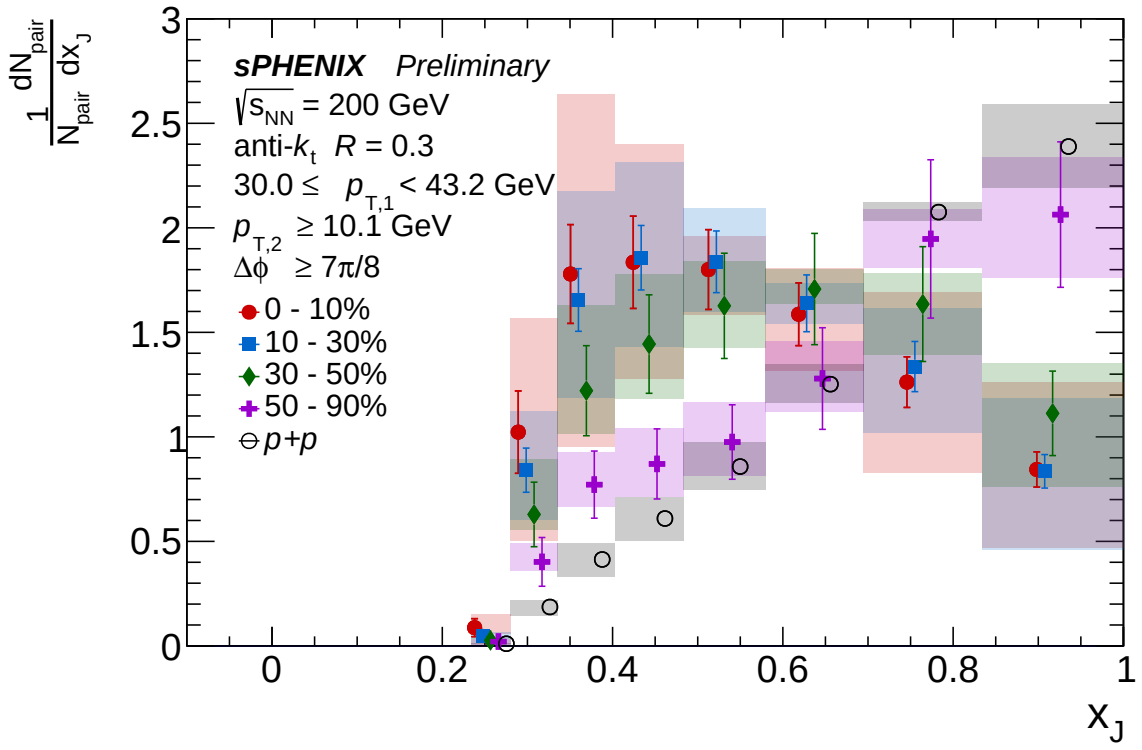

Figure 5: Fully unfolded x_J distributions of dijet events are shown for different Au+Au collision centrality intervals, 0–10%, 10–30%, 30–50%, and 50–90%, and for p+p collisions with the matching kinematic selections. Statistical uncertainties are shown as vertical lines and systematic uncertainties as filled boxes. The data points are slightly displaced horizontally within their uncertainty boxes for visibility. The 30–50% centrality interval marks the bin center. The statistical error bars for the p+p result are smaller than the markers, so they are omitted from the figure.

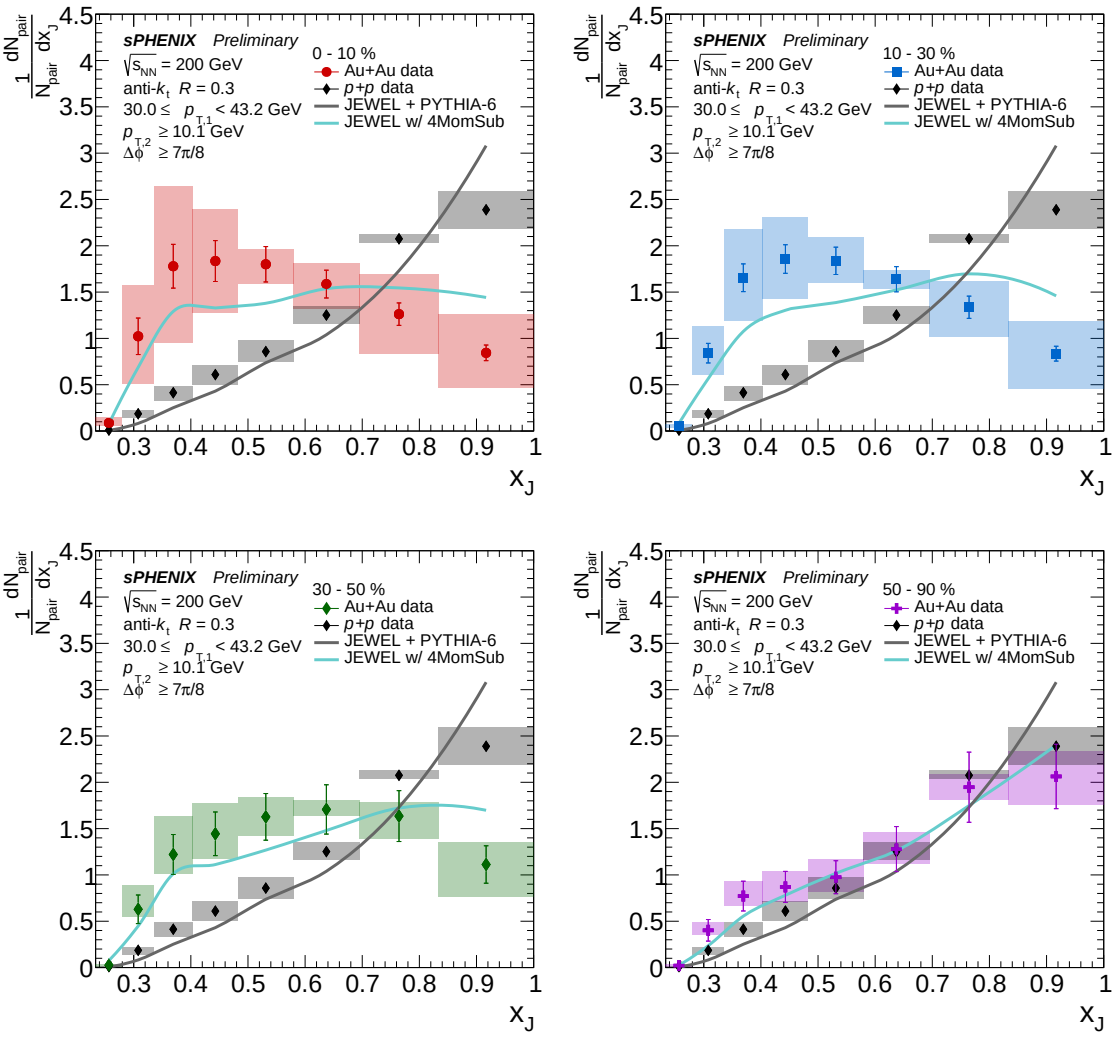

Figure 6: Fully unfolded x_J distributions of dijet events are shown for different Au+Au collision centrality intervals in each panel: 0–10%, 10–30%, 30–50%, and 50–90%. The x_J distributions in p+p collisions are shown on each panel with the matching kinematic selections. For the data distributions, statistical uncertainties are shown as vertical lines and systematic uncertainties as filled boxes. Also shown are the predictions for p+p collisions from the JEWEL + PYTHIA-6 vacuum baseline, and JEWEL + PYTHIA-6 medium results using the "4MomSub" recoil subtraction scheme.

6 Discussion

Figure 4 compares the experimental results with MC event generator simulations. The data are compared with simulations of p+p collisions from PYTHIA-8 using the Detroit tune [22]. These calculations are in close agreement with the sPHENIX p+p results and are close to agreement with the Au+Au peripheral 50–90% centrality interval results. In contrast, in the other three centrality intervals (30–50%, 10–30%, and 0–10%), the Au+Au data reveal significant modification relative to PYTHIA-8.

Figure 6 compares the data to theoretical predictions from the JEWEL (Jet Evolution With Energy Loss) MC event generator, version 2.4.0, which models jet-quenching processes in QGP [30, 31]. The simulation is based on PYTHIA-6 and then modifies the evolution of the parton shower through interactions with a medium, modeled as a two-dimensional, outwardly-expanding QGP. The code is run in "vacuum" (p+p) mode, which is based on an unofficial release of PYTHIA-6, version 6.4.25, included with the generator, and in "simple" medium mode, modeling the 0–10%, 10–30%, 30–50%, and 50–90% Au+Au centrality intervals and matching the kinematic selections in data. The medium description uses peak temperature $T_i = 375$ MeV and hydrodynamic start time $\tau_i = 0.4$ fm/c for the QGP conditions at RHIC based on Ref. [32], with other parameters set to their default values. Jets are reconstructed with the anti-k_t algorithm using $R = 0.3$ on final-state particles. For the medium output, the "4MomSub" recoil subtraction algorithm is used to remove the thermal momentum component of medium partons and thus isolate the influence of the jet energy loss [33]. Figure 6 also includes a comparison of the JEWEL calculation to all the Au+Au data centrality intervals. The JEWEL calculation with this set of parameters reproduces the qualitative features of the Au+Au data, but appears to under-predict the suppression at high x_J and the enhancement at lower x_J.

Figure 7 compares the p+p and Au+Au 0–10% centrality interval data with theoretical predictions from the Hybrid Strong/Weak Coupling Approach to Jet Quenching framework, known as the HYBRID MODEL [34]. This phenomenological model describes the modifications of jets in the QGP medium by simultaneously treating the weakly coupled physics of jet production and hard jet evolution, and the strongly coupled dynamics of the medium and the soft exchanges between the jet and the medium. The calculation results are shown with and without the inclusion of elastic scattering and with and without the inclusion of the wake, i.e., the response of the QGP fluid to energy deposited from the jet. The calculation results agree with the experimental data within uncertainties. The uncertainties on the x_J measurement presented here are larger than the differences between the calculation variations.

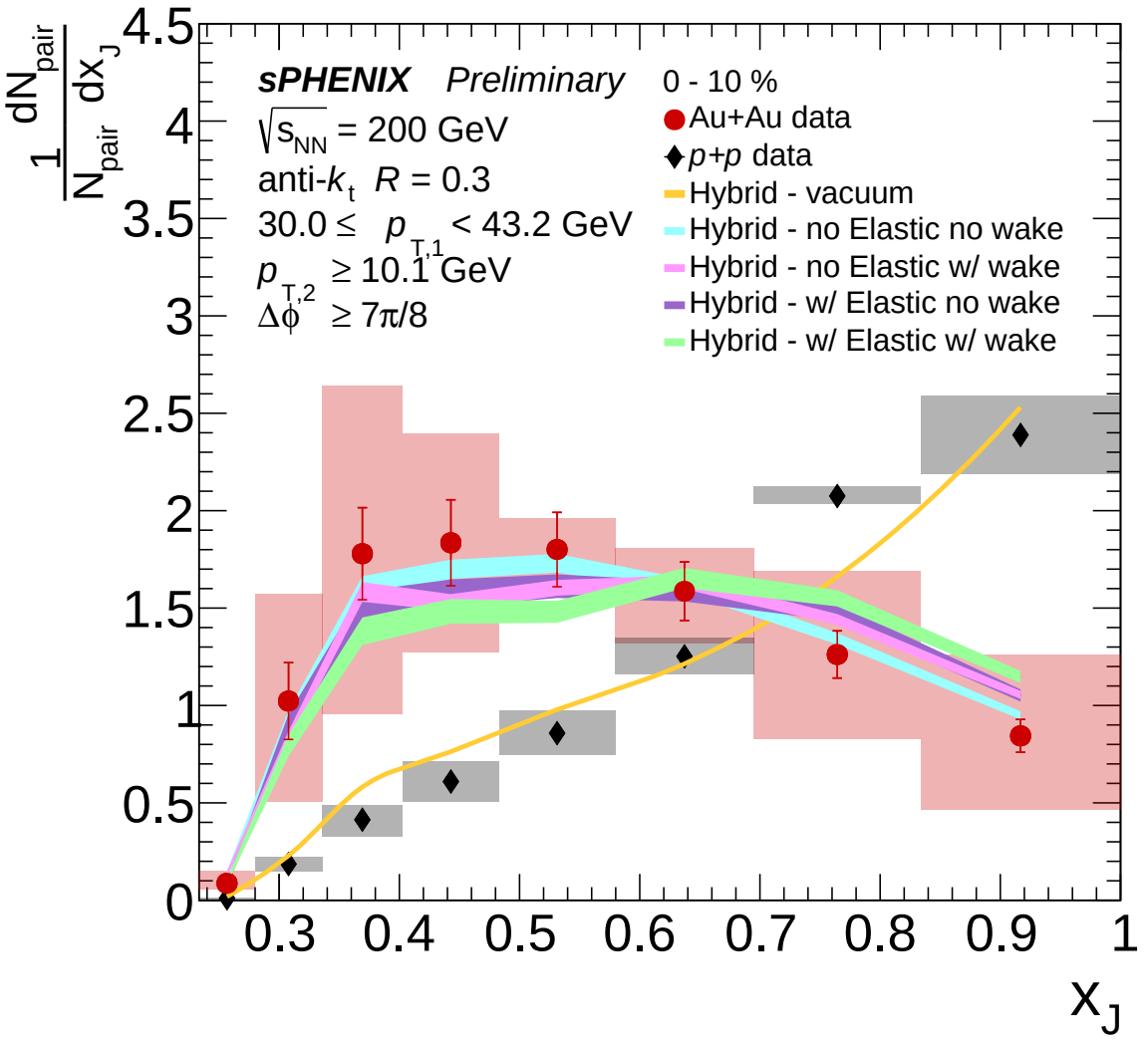

Figure 7: Fully unfolded x_J distributions of dijet events are shown for the Au+Au centrality interval 0–10%, and for p+p collisions with the matching kinematic selections. Statistical uncertainties are shown as vertical lines and systematic uncertainties as filled boxes. Also shown are HYBRID MODEL calculations with and without elastic scattering and wake effects (colored bands).

7 Summary

This note details the measurement of the dijet balance (x_J) in Au+Au and p+p collision data at $\sqrt{s_{NN}} = 200$ GeV, taken with the sPHENIX detector in 2024 at RHIC. Jets are reconstructed using the anti-k_t algorithm with $R = 0.3$ from calorimeter energy deposits. Events that contain a leading jet with $30.0 \leq p_{T,1} < 43.2$ GeV, a subleading jet with $p_{T,2} > 10.1$ GeV, and the two jets in a back-to-back configuration, $\Delta\phi > 7\pi/8$, are analyzed. The distributions of $x_J = p_{T,2}/\ p_{T,1}$ are corrected for combinatoric jet pairs and detector effects, and are reported at the truth-particle level with a per-dijet normalization. The x_J distributions are compared with the theoretical predictions from Pythia-8, Jewel, and the Hybrid Model. The x_J distributions in p+p and peripheral Au+Au 50–90% agree within uncertainties and with Pythia-8. The more central Au+Au intervals 30–50%, 10–30%, and 0–10% reveal a substantial suppression of high-x_J jet pairs and an enhancement of low-x_J pairs compared to the p+p baseline. The modifications exhibited by the jet-quenching Jewel and Hybrid Model event generators describe the general trends of the data, while the Hybrid Model provides quantitative agreement within uncertainties in the most central 0–10% collisions. Further measurements, including using the much larger Run-25 Au+Au collision dataset, are expected to explore this physics more differentially in jet kinematics and cone size, and with improved systematic control.

References

[1] Shanshan Cao and Xin-Nian Wang. Jet quenching and medium response in high-energy heavy-ion collisions: a review. *Rept. Prog. Phys.*, 84(2):024301, 2021. arXiv:2002.04028, doi:10.1088/1361-6633/abc22b. 1

[2] Georges Aad et al. Observation of a Centrality-Dependent Dijet Asymmetry in Lead-Lead Collisions at $\sqrt{s_{NN}} = 2.76$ TeV with the ATLAS Detector at the LHC. *Phys. Rev. Lett.*, 105:252303, 2010. arXiv:1011.6182, doi:10.1103/PhysRevLett.105.252303. 1

[3] Georges Aad et al. Jet radius dependence of dijet momentum balance and suppression in Pb+Pb collisions at 5.02 TeV with the ATLAS detector. *Phys. Rev. C*, 110(5):054912, 2024. arXiv:2407.18796, doi:10.1103/PhysRevC.110.054912. 1

[4] Vardan Khachatryan et al. Measurement of transverse momentum relative to dijet systems in PbPb and pp collisions at $\sqrt{s_{\rm NN}} = 2.76$ TeV. *JHEP*, 01:006, 2016. arXiv:1509.09029, doi:10.1007/JHEP01(2016)006. 1

[5] L. Adamczyk et al. Dijet imbalance measurements in $Au + Au$ and pp collisions at $\sqrt{s_{NN}} =$ 200 GeV at STAR. *Phys. Rev. Lett.*, 119(6):062301, 2017. arXiv:1609.03878, doi:10.1103/PhysRevLett.119.062301. 1

[6] Guang-You Qin and Berndt Muller. Explanation of Di-jet asymmetry in Pb+Pb collisions at the Large Hadron Collider. *Phys. Rev. Lett.*, 106:162302, 2011. [Erratum: Phys.Rev.Lett. 108, 189904 (2012)]. arXiv:1012.5280, doi:10.1103/PhysRevLett.106.162302. 1

[7] Clint Young, Bjorn Schenke, Sangyong Jeon, and Charles Gale. Dijet asymmetry at the energies available at the CERN Large Hadron Collider. *Phys. Rev. C*, 84:024907, 2011. arXiv:1103.5769, doi:10.1103/PhysRevC.84.024907. 1

[8] José Guilherme Milhano and Korinna Christine Zapp. Origins of the di-jet asymmetry in heavy ion collisions. *Eur. Phys. J. C*, 76(5):288, 2016. arXiv:1512.08107, doi:10.1140/epjc/s10052-016-4130-9. 1

[9] sPHENIX Collaboration. Measurement of dijet imbalance (x_J) and acoplanarity ($\Delta\phi$) in p+p collisions at $\sqrt{s_{NN}} = 200$ GeV with the sPHENIX detector. URL: https://www.sphenix.bnl.gov/PublicResults/sPH-CONF-JET-2025-01. 1, 3, 3, 4

[10] Matteo Cacciari, Gavin P. Salam, and Gregory Soyez. FastJet User Manual. *Eur. Phys. J. C*, 72:1896, 2012. arXiv:1111.6097, doi:10.1140/epjc/s10052-012-1896-2. 1, 3

[11] A. Adare et al. An Upgrade Proposal from the PHENIX Collaboration. 1 2015. arXiv:1501.06197. 2

[12] Ron Belmont et al. Predictions for the sPHENIX physics program. *Nucl. Phys. A*, 1043:122821, 2024. arXiv:2305.15491, doi:10.1016/j.nuclphysa.2024.122821. 2

[13] M. Harrison, T. Ludlam, and S. Ozaki. RHIC project overview. *Nucl. Instrum. Meth. A*, 499:235–244, 2003. doi:10.1016/S0168-9002(02)01937-X. 2

[14] The sPHENIX Collaboration. sPHENIX Technical Design Report, PD-2/3 Release, 2019. URL: https://indico.bnl.gov/event/7081/attachments/25527/38284/sphenixtdr20190513.pdf. 2

[15] Henry Klest. Overview and design of the sPHENIX TPC. *J. Phys. Conf. Ser.*, 1498:012025, 2020. arXiv:2110.02082, doi:10.1088/1742-6596/1498/1/012025. 2

[16] S. Aune et al. The sPHENIX Micromegas Outer Tracker. *Nucl. Instrum. Meth. A*, 1066:169615, 2024. arXiv:2403.13789, doi:10.1016/j.nima.2024.169615. 2

[17] C. A. Aidala et al. Design and Beam Test Results for the 2-D Projective sPHENIX Electromagnetic Calorimeter Prototype. *IEEE Trans. Nucl. Sci.*, 68(2):173–181, 2021. arXiv:2003.13685, doi:10.1109/TNS.2020.3034643. 2

[18] C. A. Aidala et al. Design and Beam Test Results for the sPHENIX Electromagnetic and Hadronic Calorimeter Prototypes. *IEEE Trans. Nucl. Sci.*, 65(12):2901–2919, 2018. arXiv:1704.01461, doi:10.1109/TNS.2018.2879047. 2

[19] T. G. O'Connor et al. Design and testing of the 1.5 T superconducting solenoid for the BaBar detector at PEP-II in SLAC. *IEEE Trans. Appl. Supercond.*, 9:847–851, 1999. doi:10.1109/77.783429. 2

[20] M. I. Abdulhamid et al. Measurement of the transverse energy density in Au+Au collisions at $\sqrt{s_{NN}} = 200$ GeV with the sPHENIX detector. *Phys. Rev. C*, 112(2):024908, 2025. arXiv:2504.02242, doi:10.1103/h8d5-swg6. 3

[21] Torbjörn Sjöstrand, Stefan Ask, Jesper R. Christiansen, Richard Corke, Nishita Desai, Philip Ilten, Stephen Mrenna, Stefan Prestel, Christine O. Rasmussen, and Peter Z. Skands. An introduction to PYTHIA 8.2. *Comput. Phys. Commun.*, 191:159–177, 2015. arXiv:1410.3012, doi:10.1016/j.cpc.2015.01.024. 3

[22] Manny Rosales Aguilar, Zilong Chang, Raghav Kunnawalkam Elayavalli, Renee Fatemi, Yang He, Yuanjing Ji, Dmitry Kalinkin, Matthew Kelsey, Isaac Mooney, and Veronica Verkest. Pythia8 underlying event tune for RHIC energies. *Phys. Rev. D*, 105(1):016011, 2022. arXiv:2110.09447, doi:10.1103/PhysRevD.105.016011. 3, 6

[23] Xin-Nian Wang and Miklos Gyulassy. HIJING: A Monte Carlo model for multiple jet production in pp, pA and AA collisions. *Phys. Rev. D*, 44:3501–3516, 1991. doi:10.1103/PhysRevD.44.3501. 3

[24] Jiangyong Jia and Soumya Mohapatra. Disentangling flow and nonflow correlations via Bayesian unfolding of the event-by-event distributions of harmonic coefficients in ultrarelativistic heavy-ion collisions. *Phys. Rev. C*, 88(1):014907, 2013. arXiv:1304.1471, doi:10.1103/PhysRevC.88.014907. 3

[25] B. B. Back et al. Centrality and pseudorapidity dependence of elliptic flow for charged hadrons in Au+Au collisions at $\sqrt{s_{\rm NN}} = 200$ GeV. *Phys. Rev. C*, 72:051901, 2005. arXiv:nucl-ex/0407012, doi:10.1103/PhysRevC.72.051901. 3

[26] S. Agostinelli et al. GEANT4 - A Simulation Toolkit. *Nucl. Instrum. Meth. A*, 506:250–303, 2003. doi:10.1016/S0168-9002(03)01368-8. 3

[27] J. A. Hanks et al. Method for separating jets and the underlying event in heavy ion collisions at the BNL Relativistic Heavy Ion Collider. *Phys. Rev. C*, 86:024908, 2012. arXiv:1203.1353, doi:10.1103/PhysRevC.86.024908. 3

[28] G. D'Agostini. Improved iterative Bayesian unfolding. In *Alliance Workshop on Unfolding and Data Correction*, 10 2010. arXiv:1010.0632. 3

[29] Tim Adye. Unfolding algorithms and tests using RooUnfold. In *PHYSTAT 2011*, pages 313–318, Geneva, 2011. CERN. arXiv:1105.1160, doi:10.5170/CERN-2011-006.313. 3

[30] Korinna Zapp, Gunnar Ingelman, Johan Rathsman, Johanna Stachel, and Urs Achim Wiedemann. A Monte Carlo Model for 'Jet Quenching'. *Eur. Phys. J. C*, 60:617–632, 2009. arXiv:0804.3568, doi:10.1140/epjc/s10052-009-0941-2. 6

[31] Korinna C. Zapp. JEWEL 2.0.0: directions for use. *Eur. Phys. J. C*, 74(2):2762, 2014. arXiv:1311.0048, doi:10.1140/epjc/s10052-014-2762-1. 6

[32] M. Habich, J. L. Nagle, and P. Romatschke. Particle spectra and HBT radii for simulated central nuclear collisions of C + C, Al + Al, Cu + Cu, Au + Au, and Pb + Pb from $\sqrt{s} = 62.4$ - 2760 GeV. *Eur. Phys. J. C*, 75(1):15, 2015. arXiv:1409.0040, doi:10.1140/epjc/s10052-014-3206-7. 6

[33] Raghav Kunnawalkam Elayavalli and Korinna Christine Zapp. Medium response in JEWEL and its impact on jet shape observables in heavy ion collisions. *JHEP*, 07:141, 2017. arXiv:1707.01539, doi:10.1007/JHEP07(2017)141. 6

[34] Jorge Casalderrey-Solana, Doga Can Gulhan, José Guilherme Milhano, Daniel Pablos, and Krishna Rajagopal. A Hybrid Strong/Weak Coupling Approach to Jet Quenching. *JHEP*, 10:019, 2014. [Erratum: JHEP 09, 175 (2015)]. arXiv:1405.3864, doi:10.1007/JHEP09(2015)175. 6